NANO LETTERS
Cite This: Nano Lett. 2018, 18, 1049−1056
Letter
pubs.acs.org/NanoLett

Diffusion-Controlled Epitaxy of Large Area Coalesced WSe_2 Monolayers on Sapphire

Xiaotian Zhang,[†] Tanushree H. Choudhury,[‡] Mikhail Chubarov,[‡] Yu Xiang,[§,∥] Bhakti Jariwala,[†] Fu Zhang,[†] Nasim Alem,[†,‡] Gwo-Ching Wang,[§,∥] Joshua A. Robinson,[†,‡] and Joan M. Redwing*[,†,‡]

[†]Department of Materials Science and Engineering, The Pennsylvania State University, University Park, Pennsylvania 16802, United States

[‡]2D Crystal Consortium, Materials Research Institute, The Pennsylvania State University, University Park, Pennsylvania 16802, United States

[§]Department of Physics, Applied Physics, and Astronomy, Rensselaer Polytechnic Institute, Troy, New York 12180, United States

[∥]Center for Materials, Devices, and Integrated Systems, Rensselaer Polytechnic Institute, Troy, New York 12180, United States

Supporting Information

ABSTRACT: A multistep diffusion-mediated process was developed to control the nucleation density, size, and lateral growth rate of WSe_2 domains on *c*-plane sapphire for the epitaxial growth of large area monolayer films by gas source chemical vapor deposition (CVD). The process consists of an initial nucleation step followed by an annealing period in H_2Se to promote surface diffusion of tungsten-containing species to form oriented WSe_2 islands with uniform size and controlled density. The growth conditions were then adjusted to suppress further nucleation and laterally grow the WSe_2 islands to form a fully coalesced monolayer film in less than 1 h. Postgrowth structural characterization demonstrates that the WSe_2 monolayers are single crystal and epitaxially oriented with respect to the sapphire and contain antiphase grain boundaries due to coalescence of 0° and 60° oriented WSe_2 domains. The process also provides fundamental insights into the two-dimensional (2D) growth mechanism. For example, the evolution of domain size and cluster density with annealing time follows a 2D ripening process, enabling an estimate of the tungsten-species surface diffusivity. The lateral growth rate of domains was found to be relatively independent of substrate temperature over the range of 700−900 °C suggesting a mass transport limited process, however, the domain shape (triangular versus truncated triangular) varied with temperature over this same range due to local variations in the Se/W adatom ratio. The results provide an important step toward atomic level control of the epitaxial growth of WSe_2 monolayers in a scalable process that is suitable for large area device fabrication.

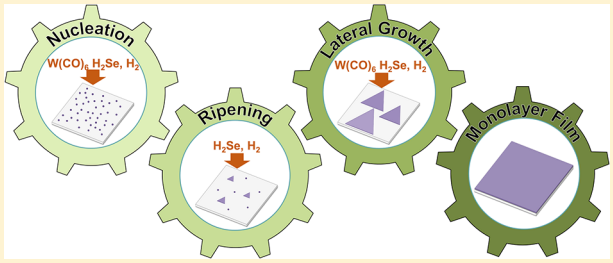

KEYWORDS: *Tungsten diselenide, chemical vapor deposition, epitaxy, ripening, surface diffusion*

Monolayer two-dimensional (2D) materials, particularly the family of transition metal dichalcogenides (TMDCs), have been a focus of increasing interest due to the limitations of zero-gap graphene and their own unique properties. For example, monolayer TMDCs such as MoS_2 and WSe_2 are direct-gap semiconductors[1] with large exciton binding energies[2,3] and thus are of interest for photonics and optoelectronics.[4,5] In addition, WSe_2 exhibits other intriguing electronic properties including native p-type conductivity,[6,7] low effective mass,[8,9] and suitable band alignment with monolayer MoS_2[10−12] for broken-gap tunnel field-effect transistors.[13] The development of device technologies based on TMDCs has, however, been hampered by difficulties in synthesizing large area monolayer and few layer films. Powder vapor transport (PVT), also referred to as powder source chemical vapor deposition (CVD), has been widely used to prepare TMDC crystal domains and films;[14,15] however, it is difficult to control and modulate the source supply in this process and uniform deposition over large substrate areas is challenging. Epitaxial TMDC films have been grown on CaF_2, epitaxial graphene, and sapphire substrates by molecular beam epitaxy (MBE)[16−21] but domain sizes are typically smaller than films grown by PVT or CVD. As a result, recent efforts have focused on the development of gas source CVD methods such as metalorganic CVD (MOCVD) for TMDCs which offers process flexibility and scalability.[22,23]

In gas source CVD, both the metal and chalcogen precursors are located outside of the deposition chamber which enables independent control of precursor partial pressures and ratios. MOCVD has been used to prepare large area, coalesced polycrystalline MoS_2, WS_2, and WSe_2 monolayer and few-layer films on a variety of substrates[22,24−26] and epitaxial growth of

Received: October 23, 2017
Revised: January 10, 2018
Published: January 17, 2018

ACS Publications © 2018 American Chemical Society

DOI: 10.1021/acs.nanolett.7b04521
Nano Lett. 2018, 18, 1049−1056

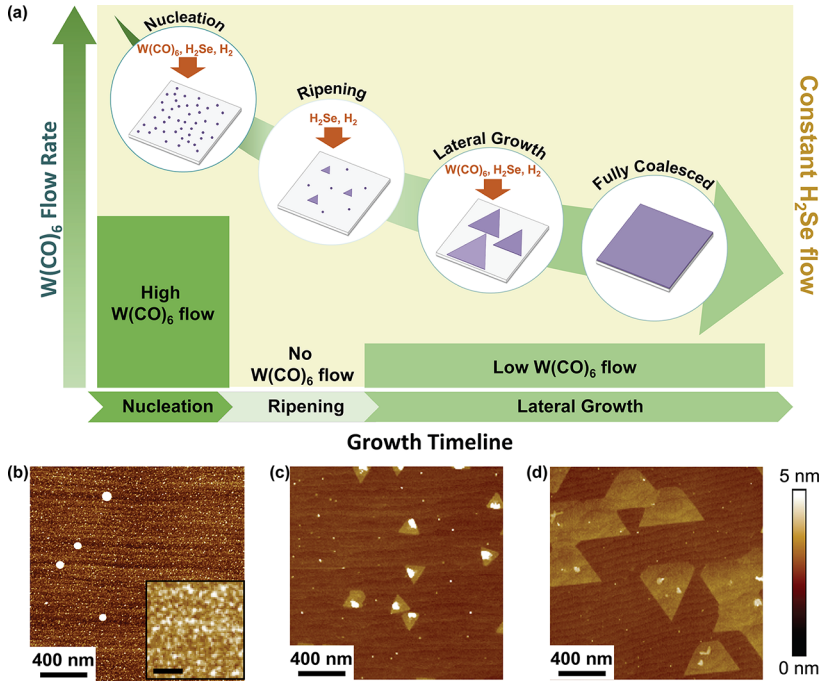

Figure 1. (a) Schematic diagram of the multistep process showing variation in $W(CO)_6$ flow rate that was used to control nucleation, ripening, and lateral growth. AFM images of WSe_2 grown on sapphire substrate (surface steps aligned horizontally) after (b) nucleation stage (inset shows the 5 times magnification of the surface, scale bar: 50 nm), (c) ripening stage, and (d) lateral growth stage.

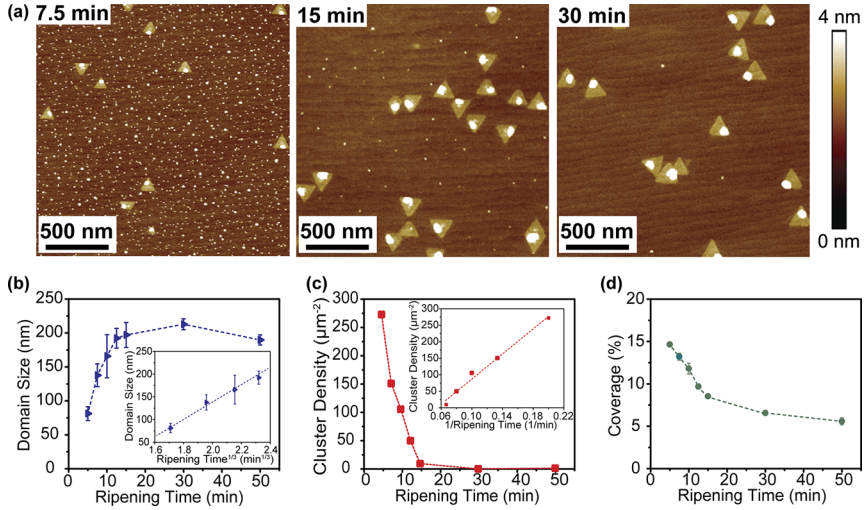

Figure 2. (a) AFM images of WSe_2 grown on sapphire substrate under 30 s nucleation time and varied ripening time for 7.5, 15, and 30 min. (b) WSe_2 domain size as a function of ripening time and cubic root of ripening time (inset). (c) Cluster density as a function of ripening time and reciprocal of ripening time (inset). (d) Substrate surface coverage as a function of ripening time.

WS_2 and WSe_2 domains by MOCVD on epitaxial graphene have been demonstrated.[23,27,28] The realization of large area single crystal TMDC monolayer films, however, requires the ability to control the density and orientation of nuclei on the substrate surface and the lateral growth rate of the domains to achieve fully coalesced 2D monolayer films with minimal 3D growth.

In this study, we demonstrate a diffusion-controlled gas source CVD process for the epitaxial growth of large area, single crystal WSe_2 monolayer and few layer films on c-plane sapphire ((0001) α-Al_2O_3). A multistep growth process was developed which employs modulation of the metal precursor partial pressure to independently control nucleation, domain ripening, lateral growth, and film coalescence via surface diffusion processes. By separating out the nucleation and lateral growth stages, the effects of process conditions on surface diffusion and lateral growth can be clearly discerned, providing insights into the fundamental processes that control WSe_2 domain growth.

A schematic of the multistep process employed in this work is shown in Figure 1 along with representative atomic force microscopy (AFM) images of the sample surface throughout the process. The WSe_2 films were synthesized by gas source chemical vapor deposition (CVD) in a cold wall vertical quartz tube reactor with an inductively heated SiC-coated graphite susceptor (Figure S1). The sapphire substrate was heated to the

DOI: 10.1021/acs.nanolett.7b04521
Nano Lett. 2018, 18, 1049−1056

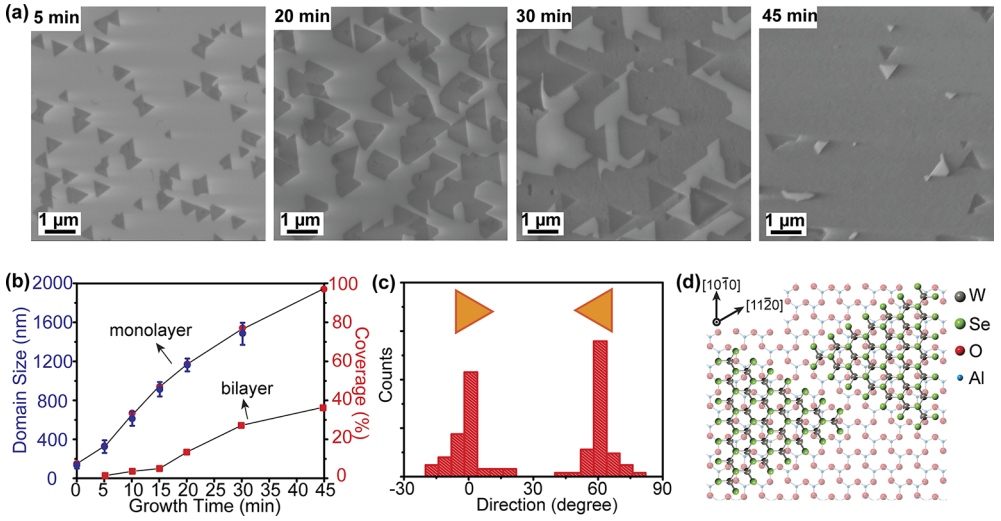

Figure 3. (a) SEM images of WSe_2 grown on sapphire substrate under 30 s nucleation time, 15 min ripening time, and varied lateral growth time for 5, 20, 30, and 45 min. (b) WSe_2 monolayer domain size and surface coverage as a function of lateral growth time and bilayer surface coverage as a function of lateral growth time. A fully coalesced monolayer WSe_2 film is achieved in ~45 min lateral growth. (c) Orientation histogram from 10 and 20 min samples confirms that WSe_2 domain edges are primarily oriented at 0° and 60° with respect to steps on sapphire. (d) Schematic illustrating 0° and 60° oriented WSe_2 domains on sapphire (0001) surface.

growth temperature of 800 °C under H_2 and exposed to H_2Se which was held at a constant flow rate of 7 sccm throughout the entire process. Tungsten hexacarbonyl ($W(CO)_6$) was initially introduced into the reactor at a higher flow rate (~1.2×10^{-3} sccm) for 30 s to drive nucleation on the sapphire surface. Immediately after this short nucleation step, a high density of W-containing nanoscale clusters (~5 nm in size) are present on the stepped sapphire surface along with a few larger particles (Figure 1b). X-ray photoelectron spectroscopy (XPS) analysis (Figure S2) suggests that the clusters are W-rich WSe_x nanoparticles, consistent with results from prior cross-section TEM analysis.[23] The $W(CO)_6$ flow was then removed from the inlet gas stream and the sample was annealed in H_2Se for 15 min. During this annealing period, the density of nanoscale clusters decreased significantly and oriented triangular WSe_2 islands with uniform size formed in a process that resembles two-dimensional ripening (Figure 1c). The $W(CO)_6$ was then reintroduced into the inlet gas at a lower flow rate than the nucleation step (~4.2×10^{-4} sccm) to limit further nucleation and promote lateral growth of the domains (Figure 1d).

The nucleation and ripening steps provide a means to control the density, size, and orientation of WSe_2 islands which is essential for achieving coalesced monolayer films. For example, the density of WSe_2 islands on the sapphire surface after 10 min ripening was found to increase approximately linearly from 4 to 60 μm^{-2} as the nucleation time was increased from 30 s to 5 min (Figure S3) for a $W(CO)_6$ flow rate of 1.2×10^{-3} sccm during the nucleation stage. The shortest nucleation time (30 s) was chosen for subsequent studies in order to achieve the largest WSe_2 domain size prior to coalescence.

A detailed study of the ripening stage provides insights into surface diffusion which is the key mechanism responsible for lateral growth of 2D monolayer domains. Figure 2a shows the WSe_2 surface morphology grown using a constant nucleation time of 30 s and increasing ripening times ranging from 7.5 to 30 min. As ripening proceeds, triangular domains start to appear with increasing density and size while the small clusters between the triangles decrease in number. The size of the triangular domains (measured by the edge length of the triangle) increases rapidly up to ~200 nm within the first 15 min of ripening (Figure 2b) with a corresponding decrease in cluster density (Figure 2c). During this same time period, the total surface coverage decreases from 15% to 8.5% (Figure 2d) mainly due to differences in the projected areas of clusters versus triangular WSe_2 domains. Beyond 15 min, the domain size, cluster density, and coverage remain relatively constant or decrease only slightly with further annealing time.

The time dependencies of the domain size and cluster density within the first 15 min are consistent with classical models of 2D ripening[29−32] whereby large particles increase in size as $t^{1/3}$ (Figure 2b inset) and small particles decrease in density as $1/t$ (Figure 2c inset). The exact mechanism by which ripening occurs is not known although it is believed to be associated with surface diffusion of W adatoms or migration of W-rich WSe_x clusters. A simplified comparison of the vapor pressures of W (<10^{-6} Torr)[33] and Se (~2750 Torr)[34] at 800 °C suggests that there should be negligible desorption of W-containing species from the surface and hence are likely the species involved in the ripening process. Tungsten-containing adatoms may diffuse from small to large clusters driven by the concentration gradient resulting from the Gibbs−Thomson effect (known as Ostwald ripening),[31] or the clusters themselves may migrate on the surface and coalesce into larger domains (known as Smoluchowski ripening),[32,35] or a combination of both processes may occur. In the case of 2D Smoluchowski ripening, the surface diffusion coefficient (D) of the clusters can be estimated based on Brownian motion and the Einstein equation $L_D = 2\sqrt{Dt}$ where L_D is the mean cluster displacement and t is the ripening time.[35] The mean cluster displacement can be approximated as $L_D \approx 1/2L_{av}$ where L_{av} is the average distance between clusters which can be estimated from the surface cluster density (N) as $L_{av} = \sqrt{(1/N)}$ (Figure S4a). The cluster density is then related to the ripening time as $1/N = 16Dt$. A plot of $(1/N)$ as a function of t (Figure S4b) shows a linear dependence in the first 10 min of ripening from which the cluster surface diffusion coefficient can be estimated as 1.2×10^{-14} cm^2/s. This value,

DOI: 10.1021/acs.nanolett.7b04521
Nano Lett. 2018, 18, 1049−1056

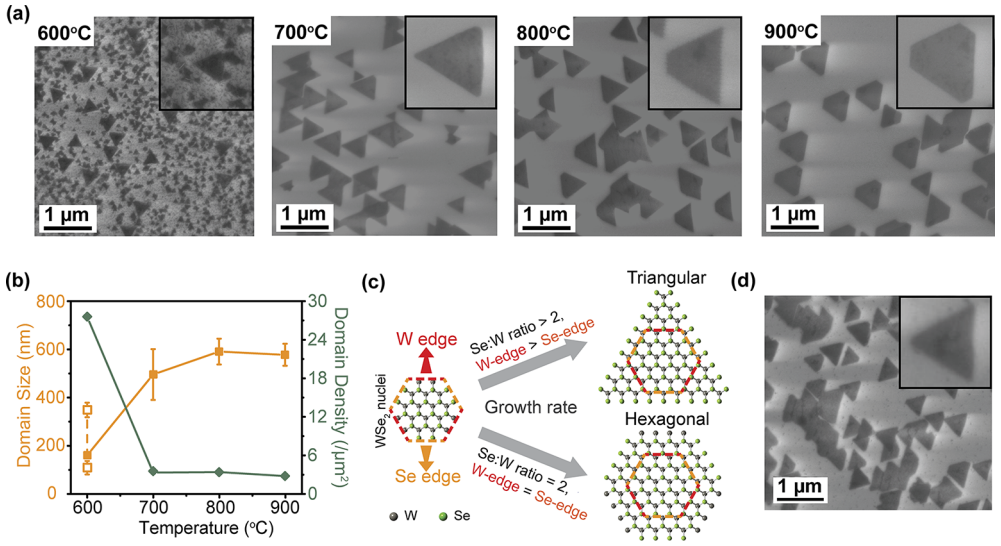

Figure 4. (a) SEM images of WSe_2 grown on sapphire substrate under 30 s of nucleation, 15 min of ripening, and 10 min of lateral growth at varied substrate temperatures of 600 °C, 700 °C, 800 °C, and 900 °C. H_2Se flow rate was held constant at 7 sccm and Se/W ratio was ~26000 during the lateral growth stage. Inset SEM images show the shape of the WSe_2 domains. (b) WSe_2 domain size and domain density as a function of substrate temperature. (c) Schematic diagram showing the variation of WSe_2 domain shape under different surface Se:W ratios. (d) SEM image of WSe_2 grown under 30 s of nucleation, 15 min of ripening, and 10 min of lateral growth at substrate temperature of 900 °C. H_2Se flow rate was increased to 10 sccm and Se/W ratio was ~37000 during the lateral growth stage. Inset SEM image shows the shape of WSe_2 domain.

which we associate with the diffusivity of the W-rich WSe_x particles, is comparable to the diffusivities of ~5 nm Pt particles on alumina (1.5×10^{-14} cm^2/s at 600 °C)[32] and ~6 nm Au particles on sapphire (2.0×10^{-14} cm^2/s at 500 °C).[36] Note that small clusters are also present on the top surface of the WSe_2 islands after ripening, typically near the edge of a domain (Figure 2a). These small clusters are similar to those present on the sapphire surface but are unable to migrate over the domain edge due to an Ehrlich-Schwoebel diffusion barrier.[37,38]

To achieve a coalesced monolayer of WSe_2, continued nucleation between or on top of the initial WSe_2 islands needs to be suppressed in order to promote lateral growth of existing domains. Therefore, following the nucleation and ripening steps, the $W(CO)_6$ precursor was reintroduced into the inlet gas stream at a lower flow rate of 4.2×10^{-4} sccm in order to reduce the gas phase supersaturation which is the driving force for crystal nucleation and growth.[39] Figure 3a shows scanning electron microscope (SEM) images of samples grown using 30 s nucleation time, 15 min ripening time, and varied lateral growth time of 5, 20, 30, and 45 min. Immediately after ripening, the domains are approximately 120 nm in size and cover 8% of the sapphire surface (t = 0 of Figure 3b). As the lateral growth time is increased, the density of triangular domains remains relatively constant and the domain size and surface coverage increase nearly linearly with lateral growth time from 5 to 15 min (Figure 3b). It should be noted that the lateral growth rate in first 5 min appears to be reduced which is likely due to a short time lag for the $W(CO)_6$ precursor to reach the substrate after it is reintroduced into the inlet gas stream. As the surface coverage increases above ~50% (15 min), however, the lateral growth rate of the monolayer decreases likely due to precursor adsorption occurring more frequently on existing WSe_2 monolayers rather than on the sapphire surface. As the WSe_2 monolayer domains increase in size, the adatoms must diffuse a longer distance to reach the domain edges, therefore, it becomes more likely that they will contribute to bilayer growth instead rather than fill in the initial monolayer. Indeed, the lateral growth rate and coverage of bilayers increases after 15 min when the monolayer lateral growth rate decreases (Figure 3b). A fully coalesced monolayer with ~36% bilayer coverage across the entire 1 cm × 1 cm sapphire substrate can be achieved in ~45 min.

The WSe_2 domains clearly exhibit preferred orientations on the (0001) sapphire surface which begins during the ripening stage (Figure 2) and is maintained throughout the lateral growth stage. A histogram (Figure 3c) of domain orientations measured after 5, 10, and 20 min of lateral growth when the domains are still isolated from each other shows two preferred orientations of 0° and 60° with respect to the step edge direction which corresponds to the $[11\bar{2}0]$ direction of sapphire, similar to that reported for epitaxial growth of MoS_2 domains on (0001) sapphire substrate by oxide powder vaporization.[40] The preferred orientation results from the commensurability between WSe_2 and sapphire (0001). Although there is large lattice mismatch between WSe_2 (a = 3.282 Å)[41] and sapphire (001) (a = 4.760 Å),[42] it is reduced to ~3.4% mismatch for 3 × 3 WSe_2 unit cells on a 2 × 2 (0001) sapphire surface (Figure 3d). Raman and room-temperature photoluminescence (PL) spectroscopy confirm the existence of monolayer WSe_2 due to the absence of a breathing mode at ~310 cm^{-1} WSe_2 (Figure S5a)[43−46] and a strong PL peak that varies from 1.60 to 1.64 eV (Figure S5b)[43] across the sample surface. Raman mapping (Figure S5c) indicates that film is largely monolayer across the 5 μm × 5 μm scan area, however, smaller scale lateral variations are evident from changes in the Raman peak intensity (Figure S5c) and PL peak position (Figure S5d). The lateral nonuniformity may arise from localized Fermi level modulations in the WSe_2 due to surface reconstruction of sapphire at the step edges,[47] and/or local variations in strain in the WSe_2 film due to tensile stress that is induced in the film upon cooldown from the growth temperature due to differences in the coefficients of thermal expansion of WSe_2 ($\alpha_a = 11.08 \times 10^{-6}$/°C)[48] and sapphire ($\alpha_a$

DOI: 10.1021/acs.nanolett.7b04521
Nano Lett. 2018, 18, 1049−1056

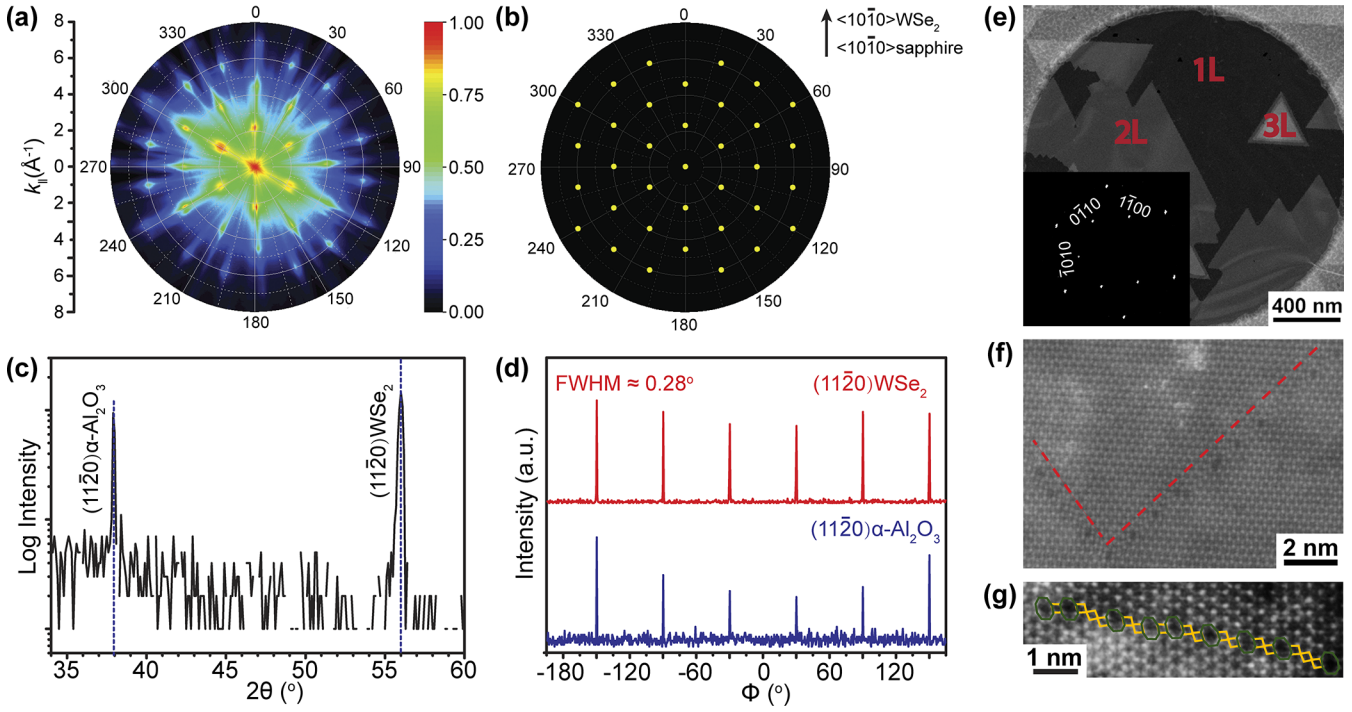

Figure 5. (a) Experimentally constructed RHEED 2D reciprocal space structure of WSe_2 plotted as the intensity ($k_{||}$) versus 360° azimuthal directions from 100 RHEED patterns recorded when the sample was rotated azimuthally with a 1.8° step size from 0° to 180° in 100 steps. (b) Theoretical simulation of 2D reciprocal space structure of WSe_2 looking along the out-of-plane [0001] direction which matches the experimental result in (a), showing [10$\bar{1}$0] WSe_2 || [10$\bar{1}$0] α-Al_2O_3. (c) θ-2θ X-ray diffractogram recorded at φ = 30° showing reflections which correspond to (11$\bar{2}$0) of WSe_2 and α-Al_2O_3. (d) φ-scan recorded at 2θ = 37.91° showing [11$\bar{2}$0] WSe_2 || [11$\bar{2}$0] α-Al_2O_3. (e) Low-magnification TEM image of coalesced WSe_2 showing single layer structure and sequent layers and the corresponding SAED pattern (inset). (f) Atomic resolution HAADF-STEM image showing the existence of antiphase grain boundaries in the film. (g) Higher-resolution HAADF-STEM image showing 4|8 rings attributed to the coalescence of 0° and 60° WSe_2 domains.

= 8.1 × 10^{-6}/°C)[49] as has been reported for CVD-grown $MoSe_2$ on SiO_2.[50]

The multistep process also provides a pathway to study the effects of growth conditions on the domain shape and lateral growth rate independent of their impact on the nucleation process. For example, Figure 4a shows the WSe_2 domain morphology after 10 min of lateral growth at 600 °C, 700 °C, 800 °C, and 900 °C with the nucleation and ripening conditions held constant (30 s of nucleation and 15 min of ripening at 800 °C) to maintain a constant initial WSe_2 domain density and size. Over the temperature range from 700 to 900 °C, the domain size and density are only weakly dependent on the growth temperature (Figure 4b) suggesting that the growth is limited by mass transport of precursors to the growth surface as is commonly observed for MOCVD growth of III−V epilayers.[51] This is reasonable considering that both $W(CO)_6$ and H_2Se are expected to decompose in the gas phase at temperatures as low as 375 °C,[52−54] consequently, WSe_2 growth is unlikely to be limited by kinetics at the growth conditions used in this study. At a lower temperature of 600 °C, however, a bimodal distribution of domain sizes was observed. The larger domains can be attributed to the initial islands formed during the nucleation and ripening stages while the smaller domains likely arise from additional nucleation occurring during the lateral growth step due to reduced surface diffusion at the lower substrate temperature. In this case, surface adatoms are likely to form new nucleation sites rather than diffuse to one of the existing WSe_2 islands and contribute to lateral growth.

The change in substrate temperature also alters the shape of the WSe_2 domains which evolves from triangular at 700 °C to truncated triangular at 900 °C (Figure 4a insets). Previous reports have demonstrated a similar shape evolution of individual MoS_2 and WSe_2 domains in PVT with respect to the source evaporation temperature,[55] substrate location relative to the source,[56] and growth temperature.[57] On the basis of these prior studies, the triangular domains shape can be attributed to the faster growth rate of W-terminated edges relative to the Se-terminated edges due to excess Se at the growth front which is expected given the high Se/W inlet gas ratio (~26,000) used in the growth process. As the growth temperature is increased, however, the W-terminated edge growth rate decreases relative to that of the Se-terminated edge resulting in truncated triangular domains which are expected to transition to a hexagonal shape when the local Se:W ratio is ~2 (Figure 4c).[56] While the Se/W inlet gas ratio remained constant in these experiments, the local Se/W ratio at the growth front is expected to be strongly temperature dependent due to the large differences in vapor pressure between Se and W which will impact surface adatom concentrations. As previously discussed, the vapor pressure of selenium is ~2750 Torr at 800 °C and increases logarithmically with temperature[58] while the vapor pressure of W remains negligibly low throughout this temperature range.[33] Consequently, the sticking coefficient of Se on the sapphire surface should decrease significantly with temperature relative to that of W resulting in a reduction in the local Se:W ratio on the surface as the temperature is increased. To test this hypothesis, the Se/W inlet gas ratio was raised from 26,000 to 37,000 for growth at

DOI: 10.1021/acs.nanolett.7b04521
Nano Lett. 2018, 18, 1049−1056

900 °C which resulted in a transition back from truncated triangular to triangular shaped domains (Figure 4d) confirming the local Se/W dependence of the domain shape.

The regular orientation of WSe_2 domains on the surface of the noncoalesced samples suggests that the film is epitaxially oriented with respect to the sapphire. This was confirmed and quantified through the use of reflection high energy electron diffraction (RHEED) analysis and in-plane X-ray diffraction (XRD) which were carried out on 1 cm × 1 cm fully coalesced monolayer films. Figure 5a shows the experimentally measured RHEED 2D reciprocal space structure of the WSe_2 monolayer plotted as the intensity $k_{\|}$ (the momentum transfer parallel to the surface) versus 360° azimuthal directions constructed from 100 RHEED patterns recorded when the sample was rotated azimuthally with a 1.8° step size from 0° to 180° in 100 steps as previously demonstrated.[59,60] The experimental RHEED 2D reciprocal space structure shows 6-fold symmetry and is consistent with the simulated pattern (Figure 5b) for WSe_2 when the out-of-plane direction is the [0001] direction, indicating that the WSe_2 monolayer is nominally single crystal with an epitaxial relation of $[10\bar{1}0]$ WSe_2 ‖ $[10\bar{1}0]$ α-Al_2O_3. The epitaxial relation was also confirmed by in-plane XRD measurements[61] which were carried out across the entire 1 cm × 1 cm sample area. The X-ray θ–2θ scan recorded using in-plane diffraction geometry at a ϕ angle where the $11\bar{2}0$ peak of α-Al_2O_3 was observed, revealed the presence of both WSe_2 and substrate $11\bar{2}0$ peaks (Figure 5c). Rotation around the surface normal fixing the 2θ angle at the $11\bar{2}0$ peaks of WSe_2 and α-Al_2O_3 (Figure 5d) shows epitaxial growth with an in-plane epitaxial relation of $[11\bar{2}0]$ WSe_2 ‖ $[11\bar{2}0]$ α-Al_2O_3 which is consistent with RHEED measurement based on the crystal symmetry of WSe_2. The measured full width at half-maximum (fwhm) of $(11\bar{2}0)$ peaks of WSe_2 in Figure 5d show a narrow value of 0.28° indicating the film is highly oriented.

High-resolution scanning transmission electron microscopy (STEM) was used to further study crystallinity and identify defects and grain boundaries in WSe_2 films removed from the sapphire substrate by a water transfer process.[62] The STEM image (Figure 5e) under low magnification and the corresponding selected area electron diffraction (SAED) pattern (Figure 5e inset) shows that the film consists of a single crystal coalesced monolayer of WSe_2 with some additional bilayer and trilayer growth. High-angle annular dark-field scanning TEM (HAADF-STEM) images (Figure 5f,g) display the atomic structure of the WSe_2 film where W and Se atoms can be identified by analyzing the intensity profile due to the Z-contrast (atomic number) characteristics in the monolayer region of WSe_2. A 60° grain boundary (GB) (mirror twin boundary) is evident in the monolayer region of WSe_2 (marked by red dashed line in Figure 5f). Figure 5g shows a higher resolution HAADF-STEM image of the 60° GB that is parallel to the zigzag geometry of the WSe_2 lattice and is stitched together by 4-fold (marked in yellow) and 8-fold (marked in green) (4|8) rings via point sharing at common Se_2 sites. This indicates the formation of antiphase boundaries that result from coalescence of 0° and 60° WSe_2 domains.[63,64]

In summary, we demonstrate a diffusion-controlled gas source CVD process for the epitaxial growth of large area, fully coalesced single crystal WSe_2 monolayer and few layer films on c-plane sapphire. A multistep growth process was developed which employs modulation of the metal precursor partial pressure to independently control nucleation, domain ripening, lateral growth, and film coalescence via surface diffusion processes. By separating out the nucleation and lateral growth stages, the effects of process conditions on nucleation density, lateral growth rate, and domain shape can be clearly distinguished, providing experimental insights into the fundamental mechanisms that control 2D domain growth. The results of this study are an important step in the development of a reproducible epitaxial growth technology for large area monolayer TMDC films and 2D heterostructures.

■ ASSOCIATED CONTENT

Supporting Information

The Supporting Information is available free of charge on the ACS Publications website at DOI: 10.1021/acs.nanolett.7b04521.

(1) Synthesis method; (2) film characterization; (3) hazards; (4) X-ray photoelectron spectroscopy; (5) nucleation density of WSe_2 islands; (6) derivation of surface diffusion coefficient; (7) Raman and photoluminescence measurements; (8) RHEED analysis of WSe_2 on sapphire (PDF)

■ AUTHOR INFORMATION

Corresponding Author

*E-mail: jmr31@psu.edu.

ORCID

Joshua A. Robinson: 0000-0001-5427-5788

Joan M. Redwing: 0000-0002-7906-452X

Notes

The authors declare no competing financial interest.

■ ACKNOWLEDGMENTS

The authors acknowledge the financial support of the Dow Chemical Company and the National Science Foundation through EFRI 2-DARE Grant EFRI-1433378 and through the Penn State 2D Crystal Consortium – Materials Innovation Platform (2DCC-MIP) under NSF cooperative agreement DMR-1539916 and Rensselaer Presidential fellowship (Y.X.). J.A.R. and B.M.P. acknowledge support from the Center for Low Energy Systems Technology (LEAST) which is one of six Semiconductor Research STARnet centers sponsored by MARCO and DARPA.

■ REFERENCES

(1) Mak, K. F.; Lee, C.; Hone, J.; Shan, J.; Heinz, T. F. Atomically Thin MoS_2: A New Direct-Gap Semiconductor. *Phys. Rev. Lett.* **2010**, *105* (13), 136805.

(2) Hanbicki, A. T.; Currie, M.; Kioseoglou, G.; Friedman, A. L.; Jonker, B. T. Measurement of High Exciton Binding Energy in the Monolayer Transition-Metal Dichalcogenides WS_2 and WSe_2. *Solid State Commun.* **2015**, *203*, 16–20.

(3) Li, Z.; Xiao, Y.; Gong, Y.; Wang, Z.; Kang, Y.; Zu, S.; Ajayan, P. M.; Nordlander, P.; Fang, Z. Active Light Control of the MoS_2 Monolayer Exciton Binding Energy. *ACS Nano* **2015**, *9* (10), 10158–10164.

(4) Baugher, B. W. H.; Churchill, H. O. H.; Yang, Y.; Jarillo-Herrero, P. Optoelectronics with Electrically Tunable PN Diodes in a Monolayer Dichalcogenide. *Nat. Nanotechnol.* **2014**, *9* (4), 262–267.

(5) Wang, Q. H.; Kalantar-Zadeh, K.; Kis, A.; Coleman, J. N.; Strano, M. S. Electronics and Optoelectronics of Two-Dimensional Transition Metal Dichalcogenides. *Nat. Nanotechnol.* **2012**, *7* (11), 699–712.

(6) Zhou, H.; Wang, C.; Shaw, J. C.; Cheng, R.; Chen, Y.; Huang, X.; Liu, Y.; Weiss, N. O.; Lin, Z.; Huang, Y.; Duan, X. Large Area Growth

DOI: 10.1021/acs.nanolett.7b04521
Nano Lett. 2018, 18, 1049–1056

and Electrical Properties of P-Type WSe_2 Atomic Layers. *Nano Lett.* **2015**, *15* (1), 709−713.
(7) Fang, H.; Chuang, S.; Chang, T. C.; Takei, K.; Takahashi, T.; Javey, A. High-Performance Single Layered WSe_2 P-FETs with Chemically Doped Contacts. *Nano Lett.* **2012**, *12* (7), 3788−3792.
(8) Wickramaratne, D.; Zahid, F.; Lake, R. K. Electronic and Thermoelectric Properties of Few-Layer Transition Metal Dichalcogenides. *J. Chem. Phys.* **2014**, *140* (12), 124710.
(9) Zhang, W.; Huang, Z.; Zhang, W.; Li, Y. Two-Dimensional Semiconductors with Possible High Room Temperature Mobility. *Nano Res.* **2014**, *7* (12), 1731−1737.
(10) Roy, T.; Tosun, M.; Cao, X.; Fang, H.; Lien, D.-H.; Zhao, P.; Chen, Y.-Z.; Chueh, Y.-L.; Guo, J.; Javey, A. Dual-Gated MoS_2/WSe_2 van Der Waals Tunnel Diodes and Transistors. *ACS Nano* **2015**, *9* (2), 2071−2079.
(11) Chiu, M.-H.; Zhang, C.; Shiu, H.-W.; Chuu, C.-P.; Chen, C.-H.; Chang, C.-Y. S.; Chen, C.-H.; Chou, M.-Y.; Shih, C.-K.; Li, L.-J. Determination of Band Alignment in the Single-Layer MoS_2/WSe_2 Heterojunction. *Nat. Commun.* **2015**, *6*, 7666.
(12) Latini, S.; Winther, K. T.; Olsen, T.; Thygesen, K. S. Interlayer Excitons and Band Alignment in MoS_2/hBN/WSe_2 van Der Waals Heterostructures. *Nano Lett.* **2017**, *17* (2), 938−945.
(13) Gong, C.; Zhang, H.; Wang, W.; Colombo, L.; Wallace, R. M.; Cho, K. Band Alignment of Two-Dimensional Transition Metal Dichalcogenides: Application in Tunnel Field Effect Transistors. *Appl. Phys. Lett.* **2013**, *103* (5), 053513.
(14) Manzeli, S.; Ovchinnikov, D.; Pasquier, D.; Yazyev, O. V.; Kis, A. 2D Transition Metal Dichalcogenides. *Nat. Rev. Mater.* **2017**, *2* (8), 17033.
(15) Shi, Y.; Li, H.; Li, L.-J. Recent Advances in Controlled Synthesis of Two-Dimensional Transition Metal Dichalcogenides via Vapour Deposition Techniques. *Chem. Soc. Rev.* **2015**, *44* (9), 2744−2756.
(16) Vishwanath, S.; Liu, X.; Rouvimov, S.; Mende, P. C.; Azcatl, A.; McDonnell, S.; Wallace, R. M.; Feenstra, R. M.; Furdyna, J. K.; Jena, D.; Grace Xing, H. Comprehensive Structural and Optical Characterization of MBE Grown $MoSe_2$ on Graphite, CaF_2 and Graphene. *2D Mater.* **2015**, *2* (2), 024007.
(17) Yue, R.; Nie, Y.; Walsh, L. A.; Addou, R.; Liang, C.; Lu, N.; Barton, A. T.; Zhu, H.; Che, Z.; Barrera, D.; Cheng, L.; Cha, P.-R.; Chabal, Y. J.; Hsu, J. W. P.; Kim, J.; Kim, M. J.; Colombo, L.; Wallace, R. M.; Cho, K.; Hinkle, C. L. Nucleation and Growth of WSe_2: Enabling Large Grain Transition Metal Dichalcogenides. *2D Mater.* **2017**, *4* (4), 045019.
(18) Nakano, M.; Wang, Y.; Kashiwabara, Y.; Matsuoka, H.; Iwasa, Y. Layer-by-Layer Epitaxial Growth of Scalable WSe_2 on Sapphire by Molecular Beam Epitaxy. *Nano Lett.* **2017**, *17* (9), 5595−5599.
(19) Liu, H. J.; Jiao, L.; Xie, L.; Yang, F.; Chen, J. L.; Ho, W. K.; Gao, C. L.; Jia, J. F.; Cui, X. D.; Xie, M. H. Molecular-Beam Epitaxy of Monolayer and Bilayer WSe_2: A Scanning Tunneling Microscopy/spectroscopy Study and Deduction of Exciton Binding Energy. *2D Mater.* **2015**, *2* (3), 034004.
(20) Zhang, Y.; Chang, T.-R.; Zhou, B.; Cui, Y.-T.; Yan, H.; Liu, Z.; Schmitt, F.; Lee, J.; Moore, R.; Chen, Y.; Lin, H.; Jeng, H.-T.; Mo, S.-K.; Hussain, Z.; Bansil, A.; Shen, Z.-X. Direct Observation of the Transition from Indirect to Direct Bandgap in Atomically Thin Epitaxial $MoSe_2$. *Nat. Nanotechnol.* **2013**, *9* (2), 111−115.
(21) Liu, H.; Chen, J.; Yu, H.; Yang, F.; Jiao, L.; Liu, G.-B.; Ho, W.; Gao, C.; Jia, J.; Yao, W.; Xie, M. Observation of Intervalley Quantum Interference in Epitaxial Monolayer Tungsten Diselenide. *Nat. Commun.* **2015**, *6*, 8180.
(22) Kang, K.; Xie, S.; Huang, L.; Han, Y.; Huang, P. Y.; Mak, K. F.; Kim, C.-J.; Muller, D.; Park, J. High-Mobility Three-Atom-Thick Semiconducting Films with Wafer-Scale Homogeneity. *Nature* **2015**, *520* (7549), 656−660.
(23) Eichfeld, S. M.; Hossain, L.; Lin, Y.; Piasecki, A. F.; Kupp, B.; Birdwell, a G.; Burke, R. a; Lu, N.; Peng, X.; Li, J.; Azcatl, A.; McDonnell, S.; Wallace, R. M.; Kim, M. J.; Mayer, T. S.; Redwing, J. M.; Robinson, J. a. Highly Scalable, Atomically Thin WSe_2 Grown via Metal−Organic Chemical Vapor Deposition. *ACS Nano* **2015**, *9* (2), 2080−2087.
(24) Kranthi Kumar, V.; Dhar, S.; Choudhury, T. H.; Shivashankar, S. A.; Raghavan, S. A Predictive Approach to CVD of Crystalline Layers of TMDs: The Case of MoS_2. *Nanoscale* **2015**, *7* (17), 7802−7810.
(25) Kim, T.; Mun, J.; Park, H.; Joung, D.; Diware, M.; Won, C.; Park, J.; Jeong, S.-H.; Kang, S.-W. Wafer-Scale Production of Highly Uniform Two-Dimensional MoS_2 by Metal-Organic Chemical Vapor Deposition. *Nanotechnology* **2017**, *28* (18), 18LT01.
(26) Kalanyan, B.; Kimes, W. A.; Beams, R.; Stranick, S. J.; Garratt, E.; Kalish, I.; Davydov, A. V.; Kanjolia, R. K.; Maslar, J. E. Rapid Wafer-Scale Growth of Polycrystalline 2H-MoS_2 by Pulsed Metal−Organic Chemical Vapor Deposition. *Chem. Mater.* **2017**, *29* (15), 6279−6288.
(27) Shi, Y.; Zhou, W.; Lu, A.-Y.; Fang, W.; Lee, Y.-H.; Hsu, A. L.; Kim, S. M.; Kim, K. K.; Yang, H. Y.; Li, L.-J.; Idrobo, J.-C.; Kong, J. Van Der Waals Epitaxy of MoS_2 Layers Using Graphene As Growth Templates. *Nano Lett.* **2012**, *12* (6), 2784−2791.
(28) Bianco, G. V.; Losurdo, M.; Giangregorio, M. M.; Sacchetti, A.; Prete, P.; Lovergine, N.; Capezzuto, P.; Bruno, G. Direct Epitaxial CVD Synthesis of Tungsten Disulfide on Epitaxial and CVD Graphene. *RSC Adv.* **2015**, *5* (119), 98700−98708.
(29) Baldan, A. Review Progress in Ostwald Ripening Theories and Their Applications to Nickel-Base Superalloys Part I: Ostwald Ripening Theories. *J. Mater. Sci.* **2002**, *37* (11), 2171−2202.
(30) Lifshitz, I. M.; Slyozov, V. V. The Kinetics of Precipitation from Supersaturated Solid Solutions. *J. Phys. Chem. Solids* **1961**, *19* (1−2), 35−50.
(31) Zinke-Allmang, M.; Feldman, L. C.; Grabow, M. H. Clustering on Surfaces. *Surf. Sci. Rep.* **1992**, *16* (8), 377−463.
(32) Wynblatt, P.; Gjostein, N. A. Supported Metal Crystallites. *Prog. Solid State Chem.* **1975**, *9* (C), 21−58.
(33) Szwarc, R.; Plante, E. R.; Diamond, J. J. Vapor Pressure and Heat of Sublimation of Tungsten. *J. Res. Natl. Bur. Stand., Sect. A* **1965**, *69A* (5), 417.
(34) Brooks, L. S. The Vapor Pressures of Tellurium and Selenium. *J. Am. Chem. Soc.* **1952**, *74* (1), 227−229.
(35) Stoldt, C. R.; Jenks, C. J.; Thiel, P. a.; Cadilhe, a. M.; Evans, J. W. Smoluchowski Ripening of Ag Islands on Ag(100). *J. Chem. Phys.* **1999**, *111* (11), 5157−5166.
(36) Beszeda, I.; Gontier-Moya, E. G.; Imre, Á. W. Surface Ostwald-Ripening and Evaporation of Gold Beaded Films on Sapphire. *Appl. Phys. A: Mater. Sci. Process.* **2005**, *81* (4), 673−677.
(37) Ehrlich, G.; Hudda, F. G. Atomic View of Surface Self−Diffusion: Tungsten on Tungsten. *J. Chem. Phys.* **1966**, *44* (3), 1039−1049.
(38) Schwoebel, R. L.; Shipsey, E. J. Step Motion on Crystal Surfaces. *J. Appl. Phys.* **1966**, *37* (10), 3682−3686.
(39) Cubillas, P.; Anderson, M. W. Synthesis Mechanism: Crystal Growth and Nucleation. In *Zeolites and Catalysis: Synthesis, Reactions and Applications*; Wiley-VCH Verlag GmbH & Co. KGaA: Weinheim, Germany, 2010; Vol. *1*, pp 1−55.
(40) Dumcenco, D.; Ovchinnikov, D.; Marinov, K.; Lazić, P.; Gibertini, M.; Marzari, N.; Sanchez, O. L.; Kung, Y.-C.; Krasnozhon, D.; Chen, M.-W.; Bertolazzi, S.; Gillet, P.; Fontcuberta i Morral, A.; Radenovic, A.; Kis, A. Large-Area Epitaxial Monolayer MoS_2. *ACS Nano* **2015**, *9* (4), 4611−4620.
(41) Schutte, W. J.; De Boer, J. L.; Jellinek, F. Crystal Structures of Tungsten Disulfide and Diselenide. *J. Solid State Chem.* **1987**, *70* (2), 207−209.
(42) Tsirelson, V. G.; Yu. Antipin, M.; Gerr, R. G.; Ozerov, R. P.; Struchkov, Y. T. Ruby Structure Peculiarities Derived from X-Ray Diffraction Data Localization of Chromium Atoms and Electron Deformation Density. *Phys. status solidi* **1985**, *87* (2), 425−433.
(43) Tonndorf, P.; Schmidt, R.; Böttger, P.; Zhang, X.; Börner, J.; Liebig, A.; Albrecht, M.; Kloc, C.; Gordan, O.; Zahn, D. R. T.; Michaelis de Vasconcellos, S.; Bratschitsch, R. Photoluminescence Emission and Raman Response of Monolayer MoS_2, $MoSe_2$, and WSe_2. *Opt. Express* **2013**, *21* (4), 4908.

DOI: 10.1021/acs.nanolett.7b04521
Nano Lett. 2018, 18, 1049−1056

(44) Zhao, Y.; Luo, X.; Li, H.; Zhang, J.; Araujo, P. T.; Gan, C. K.; Wu, J.; Zhang, H.; Quek, S. Y.; Dresselhaus, M. S.; Xiong, Q. Interlayer Breathing and Shear Modes in Few-Trilayer MoS_2 and WSe_2. *Nano Lett.* **2013**, *13* (3), 1007−1015.
(45) Del Corro, E.; Terrones, H.; Elias, A.; Fantini, C.; Feng, S.; Nguyen, M. A.; Mallouk, T. E.; Terrones, M.; Pimenta, M. A. Excited Excitonic States in 1L, 2L, 3L, and Bulk WSe_2 Observed by Resonant Raman Spectroscopy. *ACS Nano* **2014**, *8* (9), 9629−9635.
(46) Zhao, W.; Ghorannevis, Z.; Amara, K. K.; Pang, J. R.; Toh, M.; Zhang, X.; Kloc, C.; Tan, P. H.; Eda, G. Lattice Dynamics in Mono- and Few-Layer Sheets of WS_2 and WSe_2. *Nanoscale* **2013**, *5* (20), 9677.
(47) Lin, Y.-C.; Jariwala, B.; de la Bersch, B.; Xu, K.; Nie, Y.; Wang, B.; Eichfeld, S.; Zhang, X.; Choudhury, T.; Pan, Y.; Addou, R.; Smyth, C.; Li, J.; Zhang, K.; Haque, M.; Fölsch, S.; Feenstra, R.; Wallace, R.; Cho, K.; Fullerton-Shirey, S.; Redwing, J.; Robinson, J. Realizing Large-Scale, Electronic-Grade Two-Dimensional Semiconductors. *ACS Nano* **2018**, in press. http://dx.doi.org/10.1021/acsnano.7b07059.
(48) El-Mahalawy, S. H.; Evans, B. L. The Thermal Expansion of 2*H*-MoS_2, 2*H*-$MoSe_2$ and 2*H*-WSe_2 between 20 and 800°C. *J. Appl. Crystallogr.* **1976**, *9* (5), 403−406.
(49) Yim, W. M.; Paff, R. J. Thermal Expansion of AlN, Sapphire, and Silicon. *J. Appl. Phys.* **1974**, *45* (3), 1456−1457.
(50) Krustok, J.; Kaupmees, R.; Jaaniso, R.; Kiisk, V.; Sildos, I.; Li, B.; Gong, Y. Local Strain-Induced Band Gap Fluctuations and Exciton Localization in Aged WS_2 Monolayers. *AIP Adv.* **2017**, *7* (6), 065005.
(51) Biefeld, R. M.; Koleske, D. D.; Cederberg, J. G. The Science and Practice of Metal-Organic Vapor Phase Epitaxy (MOVPE). *In Handbook of Crystal Growth, 2nd Ed. Thin Films and Epitaxy: Basic Techniques, Vol. IIIA*; Kuech, T. F., Ed.; Elsevier, 2015; p 95.
(52) Haigh, J.; Burkhardt, G.; Blake, K. Thermal Decomposition of Tungsten Hexacarbonyl in Hydrogen, the Production of Thin Tungsten-Rich Layers, and Their Modification by Plasma Treatment. *J. Cryst. Growth* **1995**, *155* (3−4), 266−271.
(53) PEARSON, R.; HAUGEN, G. Kinetics of the Thermal Decomposition of H_2Se. *Int. J. Hydrogen Energy* **1981**, *6* (5), 509−519.
(54) Lewis, K. E.; Golden, D. M.; Smith, G. P. Organometallic Bond Dissociation Energies: Laser Pyrolysis of Iron Pentacarbonyl, Chromium Hexacarbonyl, Molybdenum Hexacarbonyl, and Tungsten Hexacarbonyl. *J. Am. Chem. Soc.* **1984**, *106* (14), 3905−3912.
(55) Xie, S.; Xu, M.; Liang, T.; Huang, G.; Wang, S.; Xue, G.; Meng, N.; Xu, Y.; Chen, H.; Ma, X.; Yang, D. A High-Quality Round-Shaped Monolayer MoS_2 Domain and Its Transformation. *Nanoscale* **2016**, *8* (1), 219−225.
(56) Wang, S.; Rong, Y.; Fan, Y.; Pacios, M.; Bhaskaran, H.; He, K.; Warner, J. H. Shape Evolution of Monolayer MoS_2 Crystals Grown by Chemical Vapor Deposition. *Chem. Mater.* **2014**, *26* (22), 6371−6379.
(57) Liu, B.; Fathi, M.; Chen, L.; Abbas, A.; Ma, Y.; Zhou, C. Chemical Vapor Deposition Growth of Monolayer WSe_2 with Tunable Device Characteristics and Growth Mechanism Study. *ACS Nano* **2015**, *9* (6), 6119−6127.
(58) Brebrick, R. F. Partial Pressure of Se_2 (g) in Selenium Vapor. *J. Chem. Phys.* **1968**, *48* (12), 5741−5743.
(59) Xiang, Y.; Guo, F.-W.; Lu, T.-M.; Wang, G.-C. Reflection High-Energy Electron Diffraction Measurements of Reciprocal Space Structure of 2D Materials. *Nanotechnology* **2016**, *27* (48), 485703.
(60) Tang, F.; Parker, T.; Wang, G.-C.; Lu, T.-M. Surface Texture Evolution of Polycrystalline and Nanostructured Films: RHEED Surface Pole Figure Analysis. *J. Phys. D: Appl. Phys.* **2007**, *40* (23), R427−R439.
(61) Chubarov, M.; Choudhury, T. H.; Zhang, X.; Redwing, J. M. In-Plane X-Ray Diffraction for Characterization of Monolayer and Few-Layer Transition Metal Dichalcogenide Films. *Nanotechnology* **2018**, *29* (5), 055706.
(62) Zhang, F.; Erb, C.; Runkle, L.; Zhang, X.; Alem, N. Etchant-Free Transfer of 2D Nanostructures. *Nanotechnology* **2018**, *29* (2), 025602.
(63) van der Zande, A. M.; Huang, P. Y.; Chenet, D. A.; Berkelbach, T. C.; You, Y.; Lee, G.-H.; Heinz, T. F.; Reichman, D. R.; Muller, D. A.; Hone, J. C. Grains and Grain Boundaries in Highly Crystalline Monolayer Molybdenum Disulphide. *Nat. Mater.* **2013**, *12* (6), 554−561.
(64) Zou, X.; Liu, Y.; Yakobson, B. I. Predicting Dislocations and Grain Boundaries in Two-Dimensional Metal-Disulfides from the First Principles. *Nano Lett.* **2013**, *13* (1), 253−258.

DOI: 10.1021/acs.nanolett.7b04521
Nano Lett. 2018, 18, 1049−1056